

# Learning Hybrid Actor-Critic Maps for 6D Non-Prehensile Manipulation

Wenxuan Zhou<sup>1,2</sup>, Bowen Jiang<sup>1</sup>, Fan Yang<sup>1</sup>, Chris Paxton<sup>2\*</sup>, David Held<sup>1\*</sup>

**Abstract:** Manipulating objects without grasping them is an essential component of human dexterity, referred to as non-prehensile manipulation. Non-prehensile manipulation may enable more complex interactions with the objects, but also presents challenges in reasoning about the interactions. In this work, we introduce Hybrid Actor-Critic Maps for Manipulation (HACMan), a reinforcement learning approach for 6D non-prehensile manipulation of objects using point cloud observations. HACMan proposes a *temporally-abstracted* and *spatially-grounded* object-centric action representation that consists of selecting a contact location from the object point cloud and a set of motion parameters describing how the robot will move after making contact. We modify an existing off-policy RL algorithm to learn in this hybrid discrete-continuous action representation. We evaluate HACMan on a 6D object pose alignment task in both simulation and in the real world. On the hardest version of our task, with randomized initial pose, randomized 6D goals, and diverse object categories, our policy demonstrates strong generalization to unseen object categories without a performance drop, achieving a 79% success rate on non-flat objects. Compared to alternative action representations, HACMan achieves a success rate more than three times higher than the best baseline. With zero-shot sim2real transfer, our policy can successfully manipulate unseen objects in the real world for challenging non-planar goals, using dynamic and contact-rich non-prehensile skills. Videos can be found on the project website: <https://hacman-2023.github.io>.

**Keywords:** Action Representation, Reinforcement Learning with 3D Vision, Non-prehensile Manipulation

## 1 Introduction

The ability to manipulate objects in ways beyond grasping is a critical aspect of human dexterity. Non-prehensile manipulation, such as pushing, flipping, toppling, and sliding objects, is essential for a wide variety of tasks where objects are difficult to grasp or where workspaces are cluttered or confined. However, non-prehensile manipulation remains challenging for robots. Existing work in non-prehensile manipulation faces challenges in reasoning about object geometries, contacts, and sequential decisions. Thus, previous work has only shown results with limited object generalization [1, 2, 3] or limited motion complexity, such as planar pushing or manipulating articulated objects with limited degrees of freedom [4, 5, 6]. We propose a method that generalizes across object geometries while showing versatile interactions for a complex non-prehensile manipulation task.

We present **Hybrid Actor-Critic Maps for Manipulation (HACMan)**, a reinforcement learning (RL) approach for non-prehensile manipulation with point cloud observations. The first technical contribution of HACMan is to propose an **object-centric action representation** that is **temporally-abstracted** and **spatially-grounded**. The agent selects a contact location and a set of motion parameters determining the trajectory it should take after making contact. The contact location is selected from the observed object point cloud which provides spatial grounding. At the same time, the robot decisions become more temporally-abstracted because we focus only on learning the contact-rich portions of the action.

The second technical contribution of HACMan is to incorporate the proposed action representation in an actor-critic RL framework. Since the motion parameters are defined over a continuous action space and the contact location is defined over a discrete action space (selecting a contact point among

<sup>1</sup>Robotics Institute, Carnegie Mellon University <sup>2</sup>Meta AI \*Equal Advising

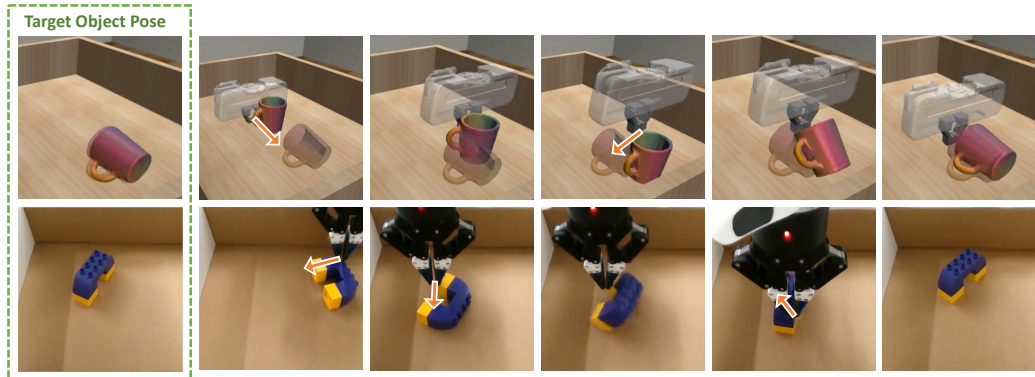


Figure 1: We propose HACMan (**H**ybrid **A**ctor-**C**ritic **M**aps for **M**anipulation), which allows non-prehensile manipulation of previously-unseen objects into arbitrary stable poses. With HACMan, the robot learns to push, tilt, and flip the object to reach the target pose, which is shown in the first column and in the top row with transparency. The policy allows for dynamic object motions with complex contact events in both simulation (top) and in the real world (bottom). The performance of the policy is best understood from the videos on the project website: <https://hacman-2023.github.io>.

the points in the object point cloud), our action representation is in a hybrid discrete-continuous action space. In HACMan, the actor network outputs *per-point* continuous motion parameters and the critic network predicts *per-point* Q-values over the object point cloud. Different from common continuous action space RL algorithms [7, 8], the per-point Q-values are not only used to update the actor, but also used as the scores when selecting the contact location. We modify the update rule of an existing off-policy RL algorithm to incorporate such a hybrid action space.

We apply HACMan to a 6D object pose alignment task with randomized initial object poses, randomized 6D goal poses, and diverse object geometries (Fig. 1). In simulation, our policy generalizes to unseen objects without a performance drop, obtaining a 79% success rate on unseen non-flat objects. In addition, HACMan achieves a training success rate more than three times higher than the best baseline with an alternative action representation. We also perform real robot experiments with zero-shot sim2real transfer where the policy shows dynamic object interactions over unseen objects of diverse shapes with non-planar goals. To summarize our contributions:

- We explore a novel object-centric action representation based on 3D spatial action maps to learn complex non-prehensile interactions. We also modify existing off-policy RL algorithm to incorporate such a hybrid discrete-continuous action space.
- The proposed action representation demonstrates substantive improvements of performance over the baselines and shows strong generalization to unseen objects.
- The learned policy showcases complex contact-rich and dynamic manipulation skills, including pushing, tilting, and flipping, shown both in simulation and with a real robot.

## 2 Related Work

**Non-prehensile manipulation.** Non-prehensile manipulation is defined as manipulating objects without grasping them [9]. Many non-prehensile manipulation tasks involve complex contact events among the robot, the object, and the environment, which lead to significant challenges in state-estimation, planning and control [1, 2, 3]. Recent work has applied learning-based methods in non-prehensile manipulation, but they are limited in terms of either skill complexity [4, 5, 6, 10] or object generalization [11, 10]. In contrast, our work shows 6D object manipulation involving more complex object interactions while also generalizing to a large variety of unseen object geometries.

**Visual Reinforcement Learning with Point Clouds.** Recent research has explored various ways of incorporating point clouds into RL [12, 13]. To overcome the optimization difficulties, previous work has tried pre-training the feature extractor with an auxiliary loss [14], initializing the RL policy with behavior cloning [15], or using privileged imitation learning [16, 17] (see detailed discussion in Appendix E). Our method does not require these additional training procedures due to the benefits of the proposed action representation. In the experiments, we show that the baselines following the most relevant previous work [12, 16] struggles when the task becomes more complex.

**Spatial action maps.** Similar to our method, recent work has explored spatial action maps that are densely coupled with visual input, based on images [18, 6, 19], point clouds [20, 5], or voxels [21]. These representations define the action space over the visual input rather than compressing it into a global embedding. Some of these papers only consider one-shot decision making (similar to a bandit problem) [5, 6] or rely on expert demonstrations with ground truth actions [18, 20, 21]. For example, Xu et al. [6] only chooses a single contact location followed by an action sequence, rather than a sequence of contact interactions. Another line of work uses spatial action maps with RL, which is the closest to our work [22, 23, 4, 19]. Most of them use DQN with a spatial action map with only discrete actions, limited to planar 2D manipulation and grasping [22, 4, 23]. In contrast, our hybrid discrete-continuous action space allows the robot to perform 3D actions without the need of discretization. Feldman et al. [19] uses a hybrid action space similar to ours, but is also limited to 2D actions with a fixed horizon of two and use images instead of point clouds. Furthermore, we demonstrate the benefit of spatial action representations when applied to a 6D non-prehensile manipulation task, which is more challenging than the pick-and-place tasks in previous work.

**RL with hybrid discrete-continuous action spaces.** Most RL algorithms focus on either a discrete action space [24] or a continuous action space [8, 7, 25]. However, certain applications are defined over a hybrid action space where the agent selects a discrete action and a continuous parameter for the action [26, 27, 28]. Unlike previous work, our hybrid action space uses a spatial action representation in which the discrete actions are defined over a map of visual inputs. The closest to our work is Feldman et al. [19] in terms of applying RL to spatial action maps, but they only consider a finite horizon of 2. We include formal definitions of the policies over the hybrid action space and modify the loss functions and exploration accordingly.

### 3 Preliminaries

A Markov Decision Process (MDP) models a sequential stochastic process. An MDP can be represented as a tuple  $(S, A, P, r)$ , where  $S$  is the state space;  $A$  is the action space;  $P(s_{t+1}|s_t, a_t)$  is the transition probability function, which models the probability of reaching state  $s_{t+1}$  from state  $s_t$  by taking action  $a_t$ ;  $r(s_t, a_t, s_{t+1})$  is the immediate reward at time  $t$ . The return  $R_t$  is defined as the cumulative discounted reward  $R_t = \sum_{i=0}^{\infty} \gamma^i r_{t+i}$ . In reinforcement learning (RL), the objective is to find a policy  $\pi(s)$  that maximizes the expected return [29]. Given a policy  $\pi$ , the Q-function is defined as  $Q^\pi(s, a) = \mathbb{E}_\pi[R_t|s_t = s, a_t = a]$ .

HACMan is built on top of Q-learning-based off-policy algorithms [7, 25, 27]. In these algorithms, we define a deterministic policy  $\pi_\theta$  parameterized by  $\theta$  and a Q-function  $Q_\phi$  parameterized by  $\phi$ . Given a dataset  $D$  with transitions  $(s_t, a_t, s_{t+1})$ , the Q-function loss is defined according to the Bellman residual:

$$L(\phi) = \mathbb{E}_{s_t, a_t, s_{t+1} \sim D} [(Q_\phi(s_t, a_t) - y_t)^2] \quad (1)$$

where  $y_t$  is defined as:

$$y_t = r_t + \gamma Q_\phi(s_{t+1}, \pi_\theta(s_{t+1})) \quad (2)$$

The policy loss for  $\pi_\theta$  is defined to maximize the Q-function:

$$J(\theta) = -\mathbb{E}_{s_t \sim D} [Q^{\pi_\theta}(s_t, a_t)|_{a_t = \pi_\theta(s)}] \quad (3)$$

### 4 Problem Statement and Assumptions

We focus on the task of 6D object pose alignment with non-prehensile manipulation. The objective for the robot is to perform a sequence of non-prehensile manipulation actions (i.e. pushing, flipping) to move an object on the table into a target goal pose. We assume that the goals are stable object poses on the table. The robot policy observes the point cloud of the scene from depth cameras, denoted as  $\mathcal{X}$ . We assume that the point cloud observation is segmented between the static background and the object to be manipulated. Thus, the full point cloud  $\mathcal{X}$  consists of the object point cloud  $\mathcal{X}^{obj}$  and the background point cloud  $\mathcal{X}^b$ .

## 5 Method

### 5.1 Action Representation

We propose an object-centric action space that consists of two parts: a **contact location**  $a^{loc}$  on an object and **motion parameters**  $a^m$  which defines how the robot moves while interacting with the object. As shown in Fig. 2, to execute an action, the end-effector will first move to a location in free space near to location  $a^{loc}$  followed by interacting with the object using the motion parameters  $a^m$ .

After the interaction, the end-effector will move away from the object, a new observation is obtained, and the next action can be taken.

Specifically, given the object point cloud  $\mathcal{X}^{obj} = \{x_i \mid i = 1 \dots N\}$ , where  $x_i \in \mathbb{R}^3$  are the point locations, the contact location  $a^{loc}$  is chosen from among the points in  $\mathcal{X}^{obj}$ . Thus,  $a^{loc}$  is a discrete action space of dimension  $N$ .

We assume a collision-free motion planner to move the gripper to the contact location  $a^{loc}$  (see Appendix A.6 for details). In contrast, the motion parameters  $a^m$ , which define how the gripper interacts with the object, are defined in a continuous action space. In this work, we define  $a^m$  as the end-effector delta position movement from the contact position, so  $a^m \in \mathbb{R}^3$ . Our experiments show that translation-only movements are sufficient to enable complex 6D object manipulation in our task.

The proposed action representation has two benefits compared to previous work. First, it is **temporally-abstracted**. Compared to the common action space of end-effector delta movement [30, 31, 11, 32], the agent with our action space can avoid wasting time learning how to move in free space and instead focus on learning contact-rich interactions. Second, it is **spatially-grounded** since the agent selects a contact location from the observed object point cloud.

## 5.2 Hybrid RL Algorithm

As discussed above, the proposed action space is a hybrid discrete-continuous action space: the contact location  $a^{loc}$  is discrete while the motion parameters  $a^m$  is continuous. We propose a way to adapt existing off-policy algorithms designed for continuous action spaces [7, 25] to this hybrid action space.

First, consider the simpler case of an action space that only has the continuous motion parameters  $a^m$ . In this case, we can directly apply existing off-policy algorithms as described in Section 3. Given the observation  $s$  (which is the point cloud  $\mathcal{X}$  in our task), we train an actor to output a vector of motion parameters  $\pi_\theta(s) = a^m$ . Similarly, the critic  $Q_\phi(s, a^m)$  outputs the Q-value given the observation  $s$  and  $a^m$ ; the Q-value is used to update the actor according to Eqn. 3.

To additionally predict the contact location  $a^{loc}$ , we also need the policy to select a point among the discrete set of points in the object point cloud  $\mathcal{X}^{obj}$ . Our insight is that we can embed such a discrete component of the action space into the critic by training the critic to output a per-point Q-value over the entire point cloud  $Q_i$ . The Q-value at each *object* point represents the estimated return after selecting this point as the contact location. These Q-values can thus be used not only to update the actor, but also to select the contact location as the point with the highest Q-value. Additionally, we train the actor to also output per-point motion parameters  $a_i^m$  for each point  $x_i$ . If point  $x_i$  is selected as the contact location  $a^{loc}$ , then the motion parameters at this point  $a_i^m$  will be used as the gripper motion after contact.

The overall architecture is shown in Fig. 3. The actor  $\pi_\theta$  receives as input the point cloud observation and outputs per-point motion parameters  $\pi_\theta(\mathcal{X}) = \{a_i^m = \pi_{\theta,i}(\mathcal{X}) \mid i = 1 \dots N\}$ . We call this per-point output an **“Actor Map”**. The critic also receives as input the point cloud observation. It first calculates per-point features  $f(\mathcal{X}) = \{f_i \mid i = 1 \dots N\}$ . The critic then concatenates each per-point feature  $f_i$  with the corresponding per-point motion parameter  $a_i^m$  and inputs the concatenated vector to an MLP. The output of the MLP is a per-point Q-value:  $Q_i = Q_\phi(f_i, a_i^m)$ , which scores the high-level action of moving the gripper to location  $x_i$  and executing motion parameters  $a_i^m$ . We call this per-point output a **“Critic Map”**. In this way, the critic is able to reason jointly about the contact location (via the feature  $f_i$ ) as well as the motion parameters  $a_i^m$ .

At inference time, we can select the point  $x_i$  within the object points  $\mathcal{X}^{obj}$  with the highest Q-value  $Q_i$  as the contact location and use the corresponding motion parameters  $a_i^m$ . For exploration during training, we define a policy  $\pi^{loc}$  which selects the contact location based on a softmax of the Q-values over all of the object points. The probability of a point  $x_i$  being selected as the contact location is thus given as:

$$\pi^{loc}(x_i \mid s) = \pi^{loc}(x_i \mid \mathcal{X}) = \exp(Q_i/\beta) / \sum_{k=1, \dots, N} \exp(Q_k/\beta) \quad (4)$$

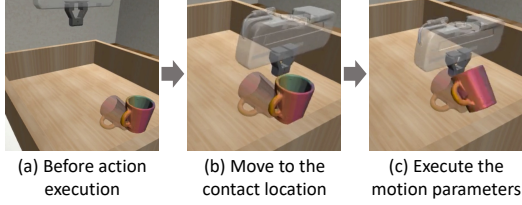


Figure 2: **Action space illustration.**

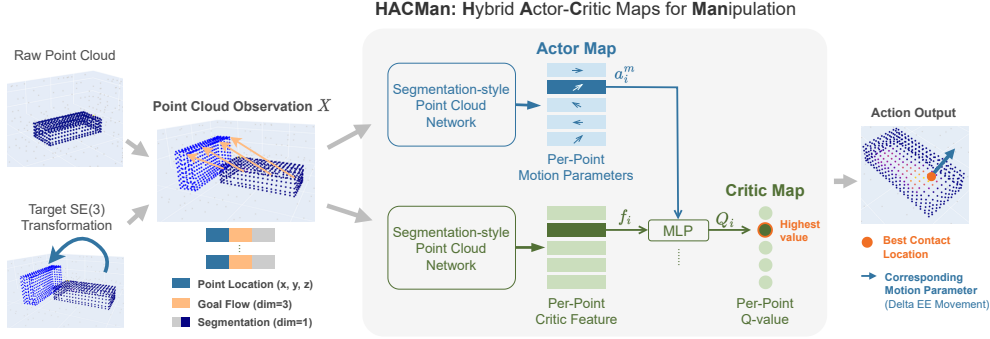


Figure 3: **An overview of the proposed method.** The point cloud observation includes the location of the points and point features. The goal is represented as per-point flow of the object points. The actor takes the observation as input and outputs an **Actor Map** of per-point motion parameters. The Actor Map is concatenated with the per-point critic features to generate the **Critic Map** of per-point Q-values. Finally, we choose the best contact location according to the highest value in the Critic Map and find the corresponding motion parameters in the Actor Map.

where  $\beta$  is the temperature of the softmax, which controls the exploration of the contact location. Note that the background points  $\mathcal{X}^b$  are included in the observation  $s = \mathcal{X} = \{\mathcal{X}^b, \mathcal{X}^{obj}\}$ , but are excluded when choosing the contact location.

We modify the update rules of the off-policy algorithm for this hybrid policy. Given  $s = \mathcal{X}$ , we first define the per-point loss for updating the actor  $\pi_{\theta,i}(s)$  at location  $x_i$  according to Eqn. 3:

$$J_i(\theta) = -Q_\phi(f_i, a_i^m) = -Q_\phi(f_i, \pi_{\theta,i}(s)) \quad (5)$$

The total objective of the actor is then computed as an expectation over contact locations:

$$J(\theta) = \mathbb{E}_{x_i \sim \pi^{loc}} [J_i(\theta)] = \sum_i \pi^{loc}(x_i | s) \cdot J_i(\theta) \quad (6)$$

where  $\pi^{loc}(x_i | s)$  is the probability of sampling contact location  $x_i$ , defined in Eq. 4. The difference between Eqn. 6 and the regular actor loss in Eqn. 3 is that we use the probability of the discrete action to weight the loss for the continuous action. To take into account  $\pi_{loc}$  during the critic update, the Q-target  $y_t$  from Eqn. 2 is modified to be:

$$y = r_t + \gamma \mathbb{E}_{x_i \sim \pi^{loc}} [Q_\phi(f_i(s_{t+1}), \pi_{\theta,i}(s_{t+1}))] \quad (7)$$

### 5.3 Representing the Goal as Per-Point Flow

As described in Section 4, our task is goal-conditioned object manipulation, in which the objective is to move an object to a given goal pose. Instead of concatenating the goal point cloud to the observed point cloud [16, 17], we represent the goal as per-point “flow” of the object point cloud to the goal: Suppose that point  $x_i$  in the initial point cloud corresponds to point  $x'_i$  in the goal point cloud; then the flow is given by  $\Delta x_i = x'_i - x_i$ . The flow  $\Delta x_i$  is a 3D vector which is concatenated to the other features of the point cloud observation. This flow representation of goal is also used to calculate the reward and success rate for the pose alignment task (Appendix A.3). In the real robot experiments, we estimate the flow using point cloud registration (Appendix D).

## 6 Experiment Setup

We evaluate our method on the 6D object pose alignment task as described in Section 4, in which the objective is for the robot to perform a sequence of non-prehensile manipulation actions (i.e. pushing, flipping) to move the object into a given goal. In this section, we describe the task setup in simulation. Details of the real robot experiments will be discussed in Section 8.

**Task Setup.** The simulation environment is built on top of Robosuite [33] with MuJoCo [34]. We consider a diverse set of objects in the simulation experiments from the Housekeep object dataset [35]. The object dataset is split into three mutually exclusive sets: training set (72 objects), unseen instances (10 objects) and unseen categories (15 objects). The 10 unseen instances consist of objects from categories included in the training set, whereas the 15 objects in “unseen categories”

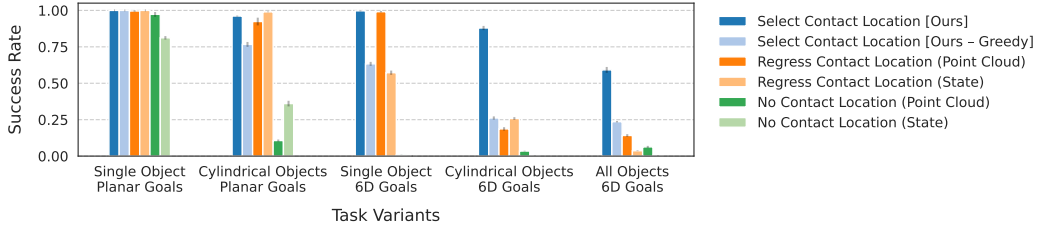


Figure 4: **Baselines and Ablations.** Our approach outperforms the baselines and the ablations, with a larger margin for more challenging tasks. Success rates for simple tasks - pushing a single object to an in-plane goal - are high for all methods, but only HACMan achieves high success rates for 6D alignment of diverse objects.

consist of novel object categories. Visualizations of the object models are included in Appendix A.1. An episode is considered as a success if the average distance of corresponding points between the object and the goal is smaller than 3 cm. Implementation details can be found in Appendix A.

**Task Variants.** To analyze the limitations of different methods, we design the object pose alignment task with varying levels of difficulty. We consider three types of object datasets: An **All Objects** dataset consists of diverse objects from Housekeep [35], a **Cylindrical Objects** dataset consisting of only cylindrical objects, and a **Single Object** dataset consists of just a single cube. We also try different task configurations: In the **Planar goals** experiments, the object starts from a *fixed* initial pose at the center of the bin, and the goal pose is a randomized *planar translation* of the starting pose. In the **6D goals** experiments, both the object initial pose and goal pose are *random SE(3)* stable poses, not limited to planar motion. This task requires SE(3) object movement to achieve the goal which imposes challenges in spatial reasoning. These different task variations are used to show at what level of difficulty each of the baseline methods stop being able to complete the task.

## 7 Simulation Results

### 7.1 Baselines and Ablations

In this section, we demonstrate the effectiveness of HACMan compared to the baselines and ablations. Fig 4 summarizes the performance of each method after being trained with the same number of environment interactions. The training curves, tables, and additional results can be found in Appendix C. Implementation details of all methods are included in Appendix B.

**Effect of action representations.** We compare our method with two alternative action representations. In **Regress Contact Location**, the policy directly regresses to a contact location and the motion parameters, instead of choosing a contact point from the point cloud as in HACMan. The **No Contact Location** baseline directly regresses to the delta end-effector movement at each timestep. For every action, the robot continues from its location from the previous action. This is the most common action space in manipulation [16, 17, 11, 12, 31, 30]. As input for these two baselines, we use either point cloud observations or ground-truth state, establishing four baselines in total. The baseline that regresses motion parameters from point cloud observations is a common action representation used in prior work in RL from point clouds, including state-of-the-art methods such as Qin et al. [12]. The baseline that regresses motion parameters from ground-truth state is the most common approach in prior work, such as in Zhou and Held [11] as well as the teacher policies in Chen et al. [16, 17] (see Appendix E for more discussion).

As shown in Fig. 4, these baseline action representations struggle with the more complex task variants. For the task variant “All Objects + 6D goals”, our method achieves a success rate 45% better than the best baseline (see Table 5 for numbers). As mentioned in Section 5, the proposed

Table 1: Features of the proposed action representation compared to the baselines.

	Spatially Grounded?	Temporally Abstracted?
Select Contact Location [Ours]	✓	✓
Regress Contact Location	×	✓
No Contact Location [16, 17, 11, 12, 31, 30]	×	×

action representation benefits from being *spatially-grounded* and *temporally-abstracted*. The comparison against the baselines demonstrates the importance of each of these two features (Table 1). The “Regress Contact Location” baseline still benefits from being temporally-abstracted because the gripper starts from a desired location for each action; however, this action representation is not spatially-grounded because it regresses to a contact location which might not be on the object surface, unlike our approach which selects the contact location among the points in the point



Figure 5: **Qualitative results for the object pose alignment task.** HACMan shows complex non-prehensile behaviors that move the object to the goal pose (shown as the transparent object).

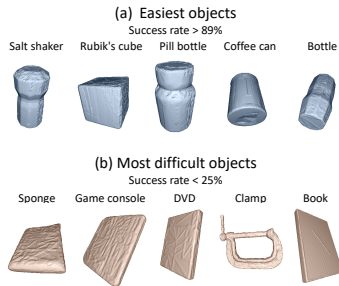


Figure 6: **Results breakdown.** Examples of the easiest and the most difficult objects. Flat and thin objects are often difficult while box-shaped and cylindrical objects have a higher success rate.

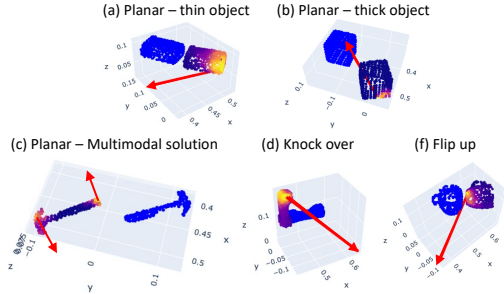


Figure 7: **Visualization of the goal-conditioned Critic Maps.** Blue: goal point cloud. Color map: observed object point cloud. Lighter colors indicate higher Critic Map scores. Red arrows: motion parameters at the specific contact location. The policy uses different contact locations based on object geometries and goals.

cloud observation. Thus, the “Regress Contact Location” baseline suffers from training difficulties with more diverse objects (last two variants in Fig. 4). The “No Contact Location” baseline is neither spatially-grounded nor temporally-abstracted; it follows the usual approach from prior work [16, 17, 11, 12, 31, 30] of regressing an end-effector delta motion at each timestep. While this is the most common action space in prior work, it has close to zero performance with 6D goals.

**Effect of Multi-step Reasoning:** To test the necessity of multi-step reasoning for the pose alignment task, we experiment with a “Greedy” version of HACMan by setting the discount factor  $\gamma$  in the RL algorithm to  $\gamma = 0$ . This forces the algorithm to optimize for greedy actions for each step. Using RL for multi-step reasoning is one of the important differences between our method and previous work such as Where2Act [5] and UMPNet [6] which optimize for one-step contact locations. Fig. 4 indicate that greedy actions might work for planar goals, but suffer from poor performance for 6D goals that requires multi-step non-greedy interactions. For example, the last row in Fig. 5 shows an example of our method pushing the object away from the goal position to prepare for flipping it to the correct orientation, demonstrating non-greedy behavior. In contrast, we find that the greedy ablation often results in local optima of only trying to match the object position but not its orientation.

## 7.2 Analysis

**Generalization to unseen objects.** The evaluation of our method over unseen objects with 6D goals is summarized in Table 2. We report the performance of the full object dataset as well as a subset of the object categories by excluding flat objects (the ratio of the second smallest dimension to the smallest dimension is larger than 1.5, more discussion in the next paragraph). Our method generalizes well to unseen object instances and unseen categories without a performance drop. Table 2 shows that, comparing the same set of object categories (“common categories”), the success rates of the training instances are similar to the unseen instances. The differences in geometry comparing the training objects and the unseen objects are visualized in Appendix A.1.

Table 2: **Generalization to unseen objects.**

Dataset	Success Rate (Flat objects excluded)	Success Rate (Full)
Train	0.789 ± .020	0.605 ± .016
Train (Common Categories)	0.852 ± .027	0.710 ± .028
Unseen Instance (Common Categories)	0.872 ± .035	0.712 ± .040
Unseen Category	0.791 ± .050	0.636 ± .034

Object Name	Planar Goals	Non-planar Goals	Total
(a) Blue cup	4/7	4/13	8/20
(b) Milk bottle	6/7	10/13	16/20
(c) Box	2/5	10/15	12/20
(d) Red bottle	4/7	0/13	4/20
(e) Hook	5/8	5/12	10/20
(f) Black mug	4/7	0/13	4/20
(g) Red mug	5/7	3/13	8/20
(h) Wood block	6/7	6/13	12/20
(i) Toy bridge	9/10	5/10	14/20
(j) Toy block	2/2	10/18	12/20
<b>Total</b>	<b>47/67</b>	<b>53/133</b>	<b>100/200</b>
<b>Percentage</b>	<b>70%</b>	<b>40%</b>	<b>50%</b>

Figure 8: **Real robot experiments.** HACMan achieves a 50% overall success rate over unseen objects with different geometries and physical properties, with 6D goal poses.

**Per-object result breakdown.** Fig. 6 visualizes the objects with the highest and the lowest success rate. The most difficult objects for this 6D pose alignment task are usually flat and thin because it is challenging to flip them to the other side using the thin edges. In contrast, the easier objects are long enough along each dimension which allows easier rotation. As shown in Table 2, by excluding flat objects, the success rate on training objects becomes 18.4% higher than the average across all categories. A histogram of per-category success rate breakdown is in Appendix C.

**Goal-conditioned Object Affordance and Multimodality.** We visualize the Critic Map, which computes the score of each contact location of the object (Fig. 7). The Critic Maps captures goal-conditioned object affordances which describe how the object can be moved to achieve the goal. Fig. 7(a) and (b) are two scenarios of performing translation object motions for different object heights: For a thin object, the Critic Map highlights the region of the top of the object (dragging) or from the back side of the object (pushing). For a thick object, it prefers to push from the bottom to avoid the object falling over. In Fig. 7(c), the hammer needs to be rotated by 180 degrees. The Critic Maps predicts a multimodal solution of pushing from either end of the object. Fig. 7(d) and (f) shows out-of-plane motions of the object of knocking over and flipping up the objects.

## 8 Real robot experiments

In the real robot experiments, we aim to evaluate the ability of the trained policy to generalize to novel objects and execute dynamic motions in the real world. We evaluate the policy with a diverse set of objects with different shapes, surface frictions, and densities (Fig. 8). We use random initial pose and random 6D goals (referred to in the previous section as “All Objects + 6D Goals”). For example, the red mug (Fig. 8(f)) has goal poses of being upright on the table or lying on the side. An episode is considered as a success if the average distance of corresponding points between the object and the goal is smaller than 3 cm; we also mark an episode as a failure if there is a failure in the point cloud registration between the observation and the goal. Implementation details of the real robot experiments can be found in Appendix D.

Fig. 8 summarizes the quantitative results of the real robot experiments. We run the evaluations without manual reset, which may create uneven numbers of planar versus out-of-plane goals. It achieves 70% success rate on planar goals and 40% success rate on non-planar goals. Non-planar goals are more difficult than the planar goals because they require dynamic motions to interact with the object. A small error in the action may result in large changes in the object movement. Videos of the real robot experiments can be found on the website: <https://hacman-2023.github.io>. The real robot experiments demonstrate that the policy is able to generalize to novel objects in the real world, despite the sim2real gap of the physics and inaccuracies of point cloud registration for estimating the goal transformation. More discussion can be found in Appendix D.

## 9 Conclusion

In this work, we propose to learn Hybrid Actor-Critic Maps with reinforcement learning for non-prehensile manipulation. The learned policy shows complex object interactions and strong generalization across unseen object categories. Limitations of our method include relying on point cloud registration to estimate the object-goal transformation, requiring relatively accurate camera calibration and the contact location being limited to observed part of the object. The proposed method has the potential to be extended and used in a wider variety of manipulation tasks. For example, we may expand the method to include not just non-prehensile actions but also grasping. We hope the proposed method and the experimental results can pave the way for future work on more skillful robot manipulation over a diverse set of objects.

## References

- [1] X. Cheng, E. Huang, Y. Hou, and M. T. Mason. Contact mode guided motion planning for quasidynamic dexterous manipulation in 3d. In *2022 International Conference on Robotics and Automation (ICRA)*, pages 2730–2736. IEEE, 2022.
- [2] Y. Hou and M. T. Mason. Robust execution of contact-rich motion plans by hybrid force-velocity control. In *2019 International Conference on Robotics and Automation (ICRA)*, pages 1933–1939. IEEE, 2019.
- [3] I. Mordatch, E. Todorov, and Z. Popović. Discovery of complex behaviors through contact-invariant optimization. *ACM Transactions on Graphics (TOG)*, 31(4):1–8, 2012.
- [4] J. Wu, X. Sun, A. Zeng, S. Song, J. Lee, S. Rusinkiewicz, and T. Funkhouser. Spatial action maps for mobile manipulation. In *Proceedings of Robotics: Science and Systems (RSS)*, 2020.
- [5] K. Mo, L. J. Guibas, M. Mukadam, A. Gupta, and S. Tulsiani. Where2act: From pixels to actions for articulated 3d objects. In *Proceedings of the IEEE/CVF International Conference on Computer Vision (ICCV)*, pages 6813–6823, October 2021.
- [6] Z. Xu, H. Zhanpeng, and S. Song. Umpnet: Universal manipulation policy network for articulated objects. *IEEE Robotics and Automation Letters*, 2022.
- [7] S. Fujimoto, H. Hoof, and D. Meger. Addressing function approximation error in actor-critic methods. In *International conference on machine learning*, pages 1587–1596. PMLR, 2018.
- [8] T. P. Lillicrap, J. J. Hunt, A. Pritzel, N. Heess, T. Erez, Y. Tassa, D. Silver, and D. Wierstra. Continuous control with deep reinforcement learning. *arXiv preprint arXiv:1509.02971*, 2015.
- [9] M. T. Mason. Progress in nonprehensile manipulation. *The International Journal of Robotics Research*, 18(11):1129–1141, 1999.
- [10] J. Liang, X. Cheng, and O. Kroemer. Learning preconditions of hybrid force-velocity controllers for contact-rich manipulation. *arXiv preprint arXiv:2206.12728*, 2022.
- [11] W. Zhou and D. Held. Learning to grasp the ungraspable with emergent extrinsic dexterity. In *Conference on Robot Learning (CoRL)*, 2022.
- [12] Y. Qin, B. Huang, Z.-H. Yin, H. Su, and X. Wang. Dexpoint: Generalizable point cloud reinforcement learning for sim-to-real dexterous manipulation. *Conference on Robot Learning (CoRL)*, 2022.
- [13] M. Liu, X. Li, Z. Ling, Y. Li, and H. Su. Frame mining: a free lunch for learning robotic manipulation from 3d point clouds. In *6th Annual Conference on Robot Learning*, 2022.
- [14] W. Huang, I. Mordatch, P. Abbeel, and D. Pathak. Generalization in dexterous manipulation via geometry-aware multi-task learning. *arXiv preprint arXiv:2111.03062*, 2021.
- [15] L. Wang, Y. Xiang, W. Yang, A. Mousavian, and D. Fox. Goal-auxiliary actor-critic for 6d robotic grasping with point clouds. In *The Conference on Robot Learning (CoRL)*, 2021.
- [16] T. Chen, J. Xu, and P. Agrawal. A system for general in-hand object re-orientation. *Conference on Robot Learning*, 2021.
- [17] T. Chen, M. Tippur, S. Wu, V. Kumar, E. Adelson, and P. Agrawal. Visual dexterity: In-hand dexterous manipulation from depth. *arXiv preprint arXiv:2211.11744*, 2022.
- [18] A. Zeng, P. Florence, J. Tompson, S. Welker, J. Chien, M. Attarian, T. Armstrong, I. Krasin, D. Duong, V. Sindhwani, and J. Lee. Transporter networks: Rearranging the visual world for robotic manipulation. *Conference on Robot Learning (CoRL)*, 2020.
- [19] Z. Feldman, H. Ziesche, N. A. Vien, and D. Di Castro. A hybrid approach for learning to shift and grasp with elaborate motion primitives. In *2022 International Conference on Robotics and Automation (ICRA)*, pages 6365–6371. IEEE, 2022.

- [20] D. Seita, Y. Wang, S. Shetty, E. Li, Z. Erickson, and D. Held. ToolFlowNet: Robotic Manipulation with Tools via Predicting Tool Flow from Point Clouds. In *Conference on Robot Learning (CoRL)*, 2022.
- [21] M. Shridhar, L. Manuelli, and D. Fox. Perceiver-actor: A multi-task transformer for robotic manipulation. In *Proceedings of the 6th Conference on Robot Learning (CoRL)*, 2022.
- [22] A. Zeng, S. Song, S. Welker, J. Lee, A. Rodriguez, and T. Funkhouser. Learning synergies between pushing and grasping with self-supervised deep reinforcement learning. In *2018 IEEE/RSJ International Conference on Intelligent Robots and Systems (IROS)*, pages 4238–4245. IEEE, 2018.
- [23] A. Hundt, B. Killeen, N. Greene, H. Wu, H. Kwon, C. Paxton, and G. D. Hager. “good robot!”: Efficient reinforcement learning for multi-step visual tasks with sim to real transfer. *IEEE Robotics and Automation Letters*, 5(4):6724–6731, 2020.
- [24] V. Mnih, K. Kavukcuoglu, D. Silver, A. Graves, I. Antonoglou, D. Wierstra, and M. Riedmiller. Playing atari with deep reinforcement learning. *arXiv preprint arXiv:1312.5602*, 2013.
- [25] T. Haarnoja, A. Zhou, P. Abbeel, and S. Levine. Soft actor-critic: Off-policy maximum entropy deep reinforcement learning with a stochastic actor. In *International conference on machine learning*, pages 1861–1870. PMLR, 2018.
- [26] M. Neunert, A. Abdolmaleki, M. Wulfmeier, T. Lampe, T. Springenberg, R. Hafner, F. Romano, J. Buchli, N. Heess, and M. Riedmiller. Continuous-discrete reinforcement learning for hybrid control in robotics. In *Conference on Robot Learning*, pages 735–751. PMLR, 2020.
- [27] M. Hausknecht and P. Stone. Deep reinforcement learning in parameterized action space. *arXiv preprint arXiv:1511.04143*, 2015.
- [28] J. Xiong, Q. Wang, Z. Yang, P. Sun, L. Han, Y. Zheng, H. Fu, T. Zhang, J. Liu, and H. Liu. Parametrized deep q-networks learning: Reinforcement learning with discrete-continuous hybrid action space. *arXiv preprint arXiv:1810.06394*, 2018.
- [29] R. S. Sutton and A. G. Barto. *Reinforcement learning: An introduction*. MIT press, 2018.
- [30] T. Mu, Z. Ling, F. Xiang, D. C. Yang, X. Li, S. Tao, Z. Huang, Z. Jia, and H. Su. Maniskill: Generalizable manipulation skill benchmark with large-scale demonstrations. In *Thirty-fifth Conference on Neural Information Processing Systems Datasets and Benchmarks Track (Round 2)*, 2021.
- [31] T. Yu, D. Quillen, Z. He, R. Julian, K. Hausman, C. Finn, and S. Levine. Meta-world: A benchmark and evaluation for multi-task and meta reinforcement learning. In *Conference on Robot Learning (CoRL)*, 2019. URL <https://arxiv.org/abs/1910.10897>.
- [32] C. R. Qi, H. Su, K. Mo, and L. J. Guibas. Pointnet: Deep learning on point sets for 3d classification and segmentation. *arXiv preprint arXiv:1612.00593*, 2016.
- [33] Y. Zhu, J. Wong, A. Mandlekar, R. Martín-Martín, A. Joshi, S. Nasiriany, and Y. Zhu. robo-suite: A modular simulation framework and benchmark for robot learning. In *arXiv preprint arXiv:2009.12293*, 2020.
- [34] E. Todorov, T. Erez, and Y. Tassa. Mujoco: A physics engine for model-based control. In *2012 IEEE/RSJ International Conference on Intelligent Robots and Systems*, pages 5026–5033. IEEE, 2012. doi:10.1109/IROS.2012.6386109.
- [35] Y. Kant, A. Ramachandran, S. Yenamandra, I. Gilitschenski, D. Batra, A. Szot, and H. Agrawal. Housekeep: Tidying virtual households using commonsense reasoning, 2022.
- [36] S. Hinterstoisser, V. Lepetit, S. Ilic, S. Holzer, G. Bradschi, K. Konolige, and N. Navab. Model based training, detection and pose estimation of texture-less 3d objects in heavily cluttered scenes. In *Computer Vision—ACCV 2012: 11th Asian Conference on Computer Vision, Daejeon, Korea, November 5–9, 2012, Revised Selected Papers, Part I 11*, pages 548–562. Springer, 2013.

- [37] Y. Xiang, T. Schmidt, V. Narayanan, and D. Fox. Posecnn: A convolutional neural network for 6d object pose estimation in cluttered scenes. *Robotics: Science and Systems (RSS)*, 2018.
- [38] T. Yu, S. Kumar, A. Gupta, S. Levine, K. Hausman, and C. Finn. Gradient surgery for multi-task learning. *Advances in Neural Information Processing Systems*, 33:5824–5836, 2020.
- [39] D. Ghosh, A. Singh, A. Rajeswaran, V. Kumar, and S. Levine. Divide-and-conquer reinforcement learning. *arXiv preprint arXiv:1711.09874*, 2017.

# Appendices

## A Simulation Environment

### A.1 Object dataset preprocessing

We use the object models from the Housekeep dataset [35]. Before importing the objects from the Housekeep dataset to MuJoCo, we perform convex decomposition using V-HACD (<https://github.com/kmammou/v-hacd>) and generate watertight meshes using Manifold (<https://github.com/hjwdzh/Manifold>). The objects are first scaled to 10 cm according to the maximum lengths along x, y, and z axis. The object sizes are randomized with an additional scale within [0.8, 1.2] for the “All Objects” task variants.

We filter out 43 objects in the Housekeep dataset due to simulation artifacts such as wall penetration and unstable contact behaviors. For example, some of the long and thin objects can be pushed into the walls and bounce back like springs. Some of the objects cannot remain stable on the table. The filtering procedure proceeds as follows: 1) we drop an object with an arbitrary quaternion and translation for 100 times; 2) we calculate the percentage of rollouts where the objects are still unstable after 80 simulation steps; 3) we filter out objects with  $> 10\%$  instability rate. After filtering, we are left with 97 objects. We split the 97 objects into three datasets, train, unseen instances, and unseen categories. The object models of the three datasets are visualized in Fig. 9, Fig. 10 and Fig. 11 respectively.

### A.2 Collecting goal poses

To collect stable goal poses, we sample a SE(3) object pose in the air above the bin, drop the object in the bin, and then wait until it becomes stable to record the pose. We collect 100 goal poses for each object. At the beginning of each episode, a goal is sampled from the list of stable poses.

### A.3 Representing the goal as per-point flow

As mentioned in Section 5.3, we represent the goal as the “flow” of each object point from the current point cloud to the corresponding point in the transformed goal point cloud. In other words, suppose that point  $x_i$  in the initial point cloud corresponds to point  $x'_i$  in the goal point cloud; then the flow is given by  $\Delta x_i = x'_i - x_i$ . The flow  $\Delta x_i$  is a 3D vector which is concatenated to the other features of the point cloud. In the ablations in Appendix C.1, we show that such a representation of the goal significantly improves training, compared to other goal representations such as concatenating the goal point cloud with the observed point cloud.

In order to compute the flow to the goal, we need to estimate correspondences between the observation and the goal. In simulation, we calculate the flow based on the ground truth correspondences, based on the known object pose. In the real robot experiments, we estimate the correspondences using point cloud registration methods (see Appendix D for details).

Further, for training the RL algorithm, we need some measure of the distance between the initial pose and the goal pose as the reward. Rather than computing a weighted average of the translation and rotation distance (which requires a weighting hyperparameter), we instead define the reward at each timestep  $r_t$  as the negative of average flow:  $r_t = -\frac{1}{N} \sum_{i=1}^N \|\Delta x_i\|$ , in which  $\|\cdot\|$  denotes the L2 distance. This computation is similar to the “matching score” [36] or “PLoss” [37] used in previous work, except here we use it as a reward function.

### A.4 Success rate definition

An episode is marked as a success when the average distance of the corresponding points between the object and the goal is smaller than 3 cm. More specifically, this is calculated by the average norm of the per-point flow vectors as described in Appendix A.3. The episode terminates when it reaches a success. If the episode does not reach a success within 10 steps, it is marked as a failure.

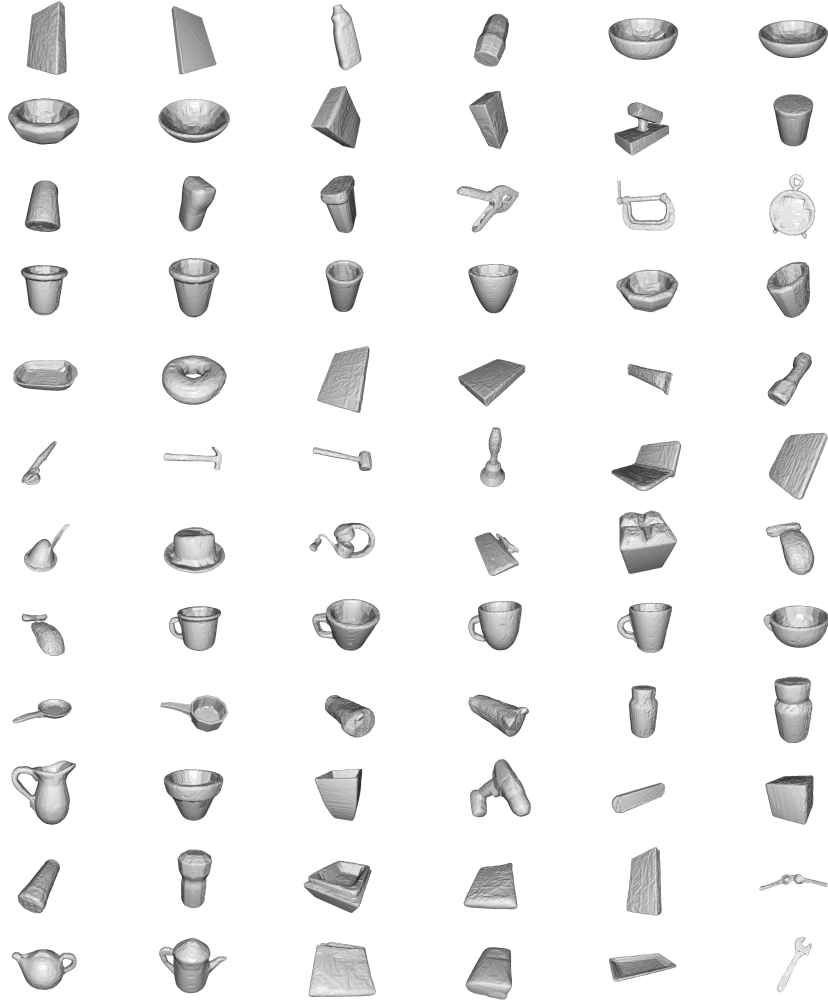


Figure 9: **Training objects.** 72 Housekeep objects used in training.

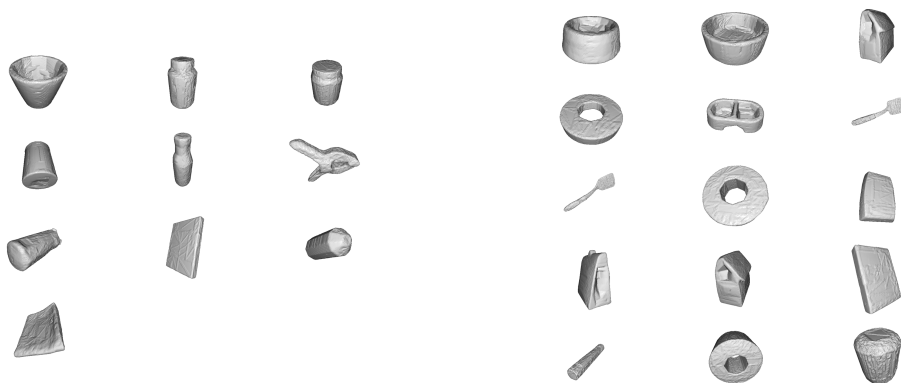


Figure 10: **Evaluation objects (unseen instance).** 10 Housekeep objects used in unseen instance evaluations. Each instance is selected from an object category with equal or more than three instances.

Figure 11: **Evaluation objects (unseen category).** 15 Housekeep objects used in unseen category evaluations. 8 categories are randomly chosen.

## A.5 Observation

The observation space includes a point cloud of the entire scene  $\mathcal{X}$ . It contains background points  $\mathcal{X}^b$  and object points  $\mathcal{X}^{obj}$ . Note that we move the gripper to a reset pose after every action before taking the next observation. Thus, the gripper is not observed in the point cloud. To get the point cloud, we set three cameras around the bin (Fig. 12). The depth readings from the cameras are converted to a set of point locations in the robot base frame and combined.

The object points are then downsampled with a voxel size of  $0.005 \text{ m} \times 0.005 \text{ m} \times 0.005 \text{ m}$  and the background points are downsampled with a voxel size of  $0.02 \text{ m} \times 0.02 \text{ m} \times 0.02 \text{ m}$ . We empirically find that using a slightly denser object point cloud may increase the performance.

More specifically, using a  $0.005 \text{ m} \times 0.005 \text{ m} \times 0.005 \text{ m}$  voxel downsample is slightly better than  $0.01 \text{ m} \times 0.01 \text{ m} \times 0.01 \text{ m}$ . We suspect that the policy can perform more delicate manipulation of the object with a denser point cloud. The PointNet++ segmentation architecture could be sufficiently efficient in terms of generalization across nearby points, thus a dense point cloud might not lead to worse sample efficiency.

After downsampling, we estimate the normals of the object points using Open3D ([http://www.open3d.org/docs/0.7.0/python\\_api/open3d.geometry.estimate\\_normals.html](http://www.open3d.org/docs/0.7.0/python_api/open3d.geometry.estimate_normals.html)). The estimated normals will be used during action execution (discussed in the next section).

As mentioned in Fig. 3, the feature of each point contains the goal flow and the segmentation mask. The goal flow of the object point is calculated according to Section A.3. The goal flow of the background point is set to zero. We obtain the segmentation labels of the object points and the background points from Robosuite [33].

## A.6 Action

As mentioned in Section 5, the proposed method uses an action space with a contact location selected from the object points and a set of motion parameters. We discuss the implementation details of executing such an action in the simulation environment in this section. Note that we use a floating gripper as the robot in simulation since we only focus on gripper interactions with the objects.

Once the policy selects a point on the object point cloud, we obtain the corresponding location and estimated normal of the point as described in the previous section. The robot first moves to a “pre-contact” location which is 2 cm away from the contact location along the surface normal. This is implemented by directly setting the gripper to the desired pose. If the gripper encounters a collision at the desired pose, we mark this action as failure and skip the remaining action execution procedure. After reaching the pre-contact location, the gripper will approach to the desired contact location using a low-level controller. After that, the robot will execute the motion parameters which is the end-effector delta position command. We did not consider the change of gripper orientation because the delta position command leads to sufficiently complex object motion in our experiments. We use an action scale of 2 cm and the action command is executed with an action repeat of 3. We use Operation Space Controller with relatively low gains to allow compliant contact-rich motions with the object.

The gripper may not exactly reach the desired location in both sim and real, due to the compliant low-level controller and the gripper geometry. We take this imperfect execution into account during training as a part of the environment dynamics. We do not enforce assumptions such as keeping the contact while executing the motion parameter or avoiding other contact points. Avoiding such assumptions on contacts is a strength of the proposed method compared to some of the classical methods [1, 2].

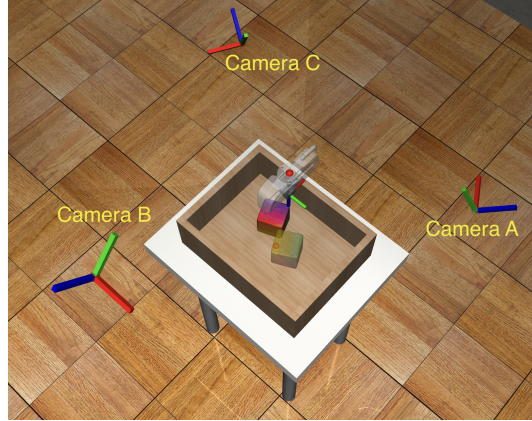


Figure 12: Camera locations in simulation.

## B Algorithm and Training Details

### B.1 HACMan (Ours)

HACMan is modified on top of TD3 [7] based on the implementation from Stable-Baselines3 (<https://github.com/DLR-RM/stable-baselines3>). We use PointNet++ segmentation-style backbones for both the actor and the critic using the implementation from PyG (<https://pytorch-geometric.readthedocs.io>). Note that the backbones are not shared between the actor and the critic. Hyperparameters are included in Table 3. The actor and the critic use the same network size and the same learning rate. To improve the stability of policy training, we clamp the target Q-values according to an estimated upper bound and lower bound of the return for the task. The location policy temperature  $\beta$  is described in Eqn 4.

Table 3: Hyperparameters.

Hyperparameters	Values
Initial timesteps	10000
Batch size	64
Discount factor ( $\gamma$ )	0.99
Critic update freq per env step	2
Actor update freq per env step	0.5
Target update freq per env step	0.5
Learning rate	0.0001
MLP size	[128, 128, 128]
Critic clamping	[-20, 0]
Location policy temperature ( $\beta$ )	0.1

### B.2 Baselines

The baselines share the same code framework as HACMan. We discuss their differences with HACMan in this section.

**Regress Contact Location.** Unlike HACMan, this baseline does not refer to the object surface for contact point selection. Instead, it directly predicts a location (dim=3) and a motion parameter (dim=3, delta-EE movement). For each action execution, the end-effector approaches the location, moves according to the motion parameters, and resets to the default pose. To improve the performance of this baseline, we map the contact location output to be within the bounding box of the object. Since the location output is no longer a point selected from the object surface, the surface normal vector used in HACMan becomes unavailable. Instead, this baseline always approaches the location from the top at a height equal to the maximum side length of the object bounding box.

**No Contact Location.** This baseline does not leverage the contact point concept - it only predicts a motion parameter (dim=3, delta-EE movement). For each action execution, the end-effector moves according to the motion parameter starting from where it ends after the previous action, without resetting to the default pose. To reduce the exploration difficulties, we make two additional changes: 1) we always start the end-effector right above the object (at a height equal to the maximum side length of the object bounding box) at the beginning of an episode, and 2) we add an extra term to the reward function that penalizes the end-effector for being too far from the object,

$$J_{\text{dist}} = \begin{cases} -\lambda_{\text{dist}}(d_{\text{min}} - 0.05), & d_{\text{min}} > 0.05 \text{ m} \\ 0, & \text{otherwise} \end{cases} \quad (8)$$

where  $d_{\text{min}}$  is the minimum distance from the end-effector to the object point cloud vertices, and  $\lambda_{\text{dist}}$  is the weight for this reward term.

**Point Cloud.** Unlike HACMan, the points baselines use PointNet++ classification-style backbones from PyG (<https://pytorch-geometric.readthedocs.io>). For each point cloud, it extracts a single global feature vector instead of per-point feature.

**State.** In the states baselines, the input consists of the pose of the current object, the goal, and optionally the end-effector if the baseline is using “No Contact Location”. Each pose is a vector (dim=7) that consists of a translation (dim=3) and a quaternion (dim=4). The model concatenates all the pose vectors into a single vector as the input to an MLP.

We report the best results of the baselines in the paper by searching over different hyperparameters for each baseline, including learning rate, actor update frequency, initial timesteps, and EE distance weight  $\lambda_{dist}$ . The best hyperparameters for each baseline that are different from HACMan are summarized in Table 4.

Table 4: Baseline-specific Hyperparameters.

Baselines	Hyperparameters	Values
Regress Contact Location (Point Cloud)	Actor update freq per env step	0.25
No Contact Location (Point Cloud)	Actor update freq per env step	0.25
	EE Distance Weight $\lambda_{dist}$	1
No Contact Location (State)	EE Distance Weight $\lambda_{dist}$	5

## C Supplementary Experiment Results

### C.1 Additional ablations

We perform additional ablation studies to analyze each component of the proposed method with all the variants of the object pose alignment task. The results of the ablations are summarized in Fig. 13.

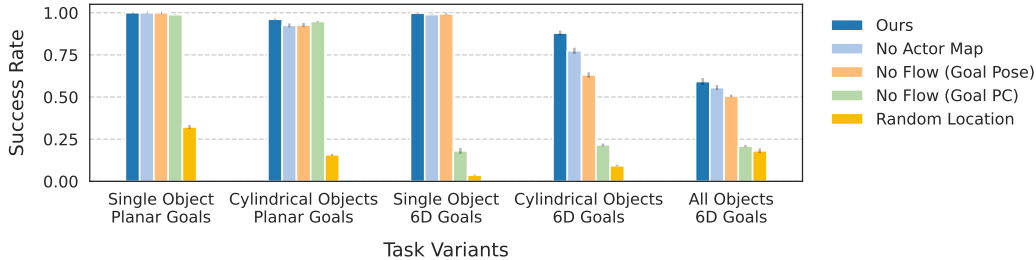


Figure 13: **Additional ablations.** All of the components are essential to achieve the best performance when the task becomes more difficult.

**Effect of Contact Location:** To test the hypothesis that contact location matters for non-prehensile manipulation, we design a “**Random Location**” ablation: the policy randomly selects a contact location on the object instead of learning to predict a contact location. From Fig. 13, we observe a performance drop for not predicting the contact location even for the simplest task variant.

**Effect of Correspondence Flow in Observations:** As described in Section 5.3 and Appendix A.3, in our method, we represent the goal by first computing the correspondence between the observation and goal point clouds and inputting a per-point “flow” to the goal. We include two alternative goal representations to justify the use of flow in our pipeline: “**No Flow (Goal PC)**” concatenates the goal point cloud with the observed point cloud [16, 17]. We use an additional segmentation label in the point features to distinguish the goal points from the observed points. From Fig. 13, this ablation only works well on planar goals for this task. In “**No Flow (Goal Pose)**”, we include the goal pose as features for all the object points. The goal pose is represented as a 7D vector that includes a translation vector and a quaternion. It is worse than our method in the last two task variants.

**Effect of Actor Map:** Instead of using an Actor Map which has per-point outputs, this ablation uses an actor that outputs a single vector of motion parameters while keeping the Critic Map. This is different from the baselines in the previous section that remove both the Actor and Critic Maps. In the “**No Actor Map**” experiments, we observe a relatively minor performance difference compared to the full method. Using the per-point action output from an Actor Map instead of a single output may allow the agent to reason more effectively about different actions for different contact locations, such as the multimodal solution shown in Fig. 7 (middle).

### C.2 Training curves and tables

In this section, we include the full training results for all the methods with additional task variants. Fig. 14 and Fig. 15 include the training curves for the baselines and the ablations. Table 5 and Table 6 are recorded at 200k environment interaction steps from the training curves for all the methods. The numbers in the tables are used to generate the bar plots in Fig. 4 and Fig. 13.

Note that we use different names for the task configurations compared to the main paper to include additional task variants. “Fixed Init - Translation Goal” corresponds to the “Planar Goals” in the main paper and “Any Init - Any Goal” corresponds to the “6D Goals”. We also interpolate between these two task configurations and include an additional task configuration with a fixed initial object pose and a randomized 6D goal, “Fixed Init - Any Goal”. This task configuration is combined with the Single Object dataset and the Cylindrical Object dataset. Thus, we include 7 variants in total (5 variants in the main paper).

As discussed in Section 7, the baselines and ablations have poor performance when the task becomes more challenging. Our method achieves the best converged performance across all task variants while being more sample efficient.

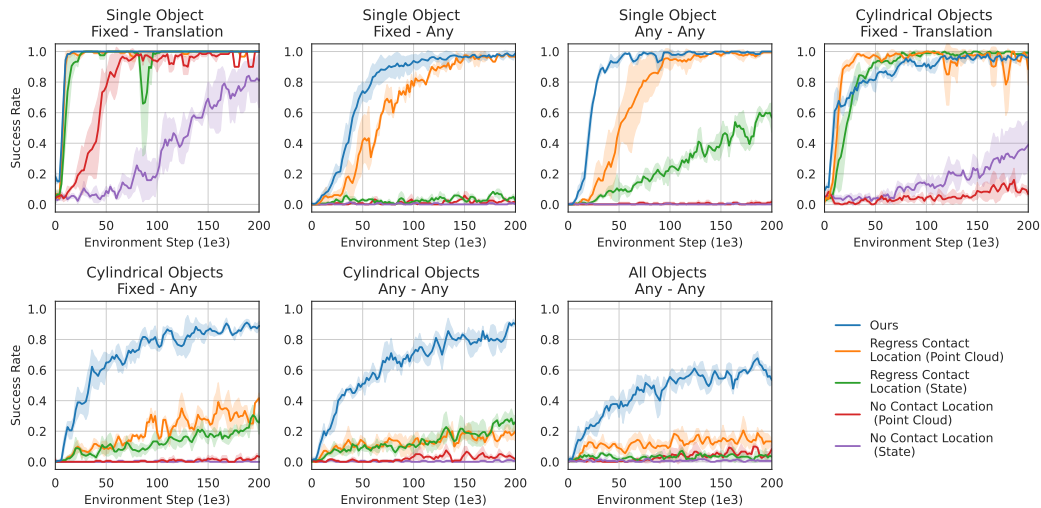


Figure 14: **Baselines.** Note that **Fixed Init - Translation Goal** and **Any Init - Any Goal** correspond to **Planar Goals** and **6D Goals** in Fig. 4 respectively. The shaded area represents the standard deviation across three training seeds.

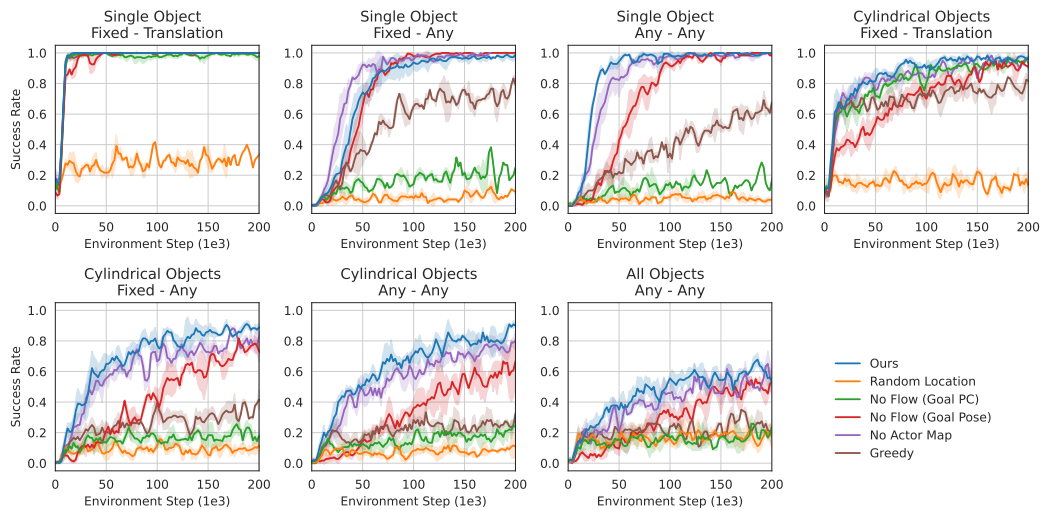


Figure 15: **Ablations.** Note that **Fixed Init - Translation Goal** and **Any Init - Any Goal** correspond to **Planar Goals** and **6D Goals** in Fig. 13 respectively. The shaded area represents the standard deviation across three training seeds.

Table 5: **Baselines.** We compare our method with baselines with different action representations and observations. Our approach outperforms the baselines, with a larger margin for more challenging tasks. The success rate is reported with the mean and standard deviation across three seeds. Note that **Fixed Init - Translation Goal** and **Any Init - Any Goal** correspond to **Planar Goals** and **6D Goals** in Fig. 4 respectively.

Object Dataset	Task Configuration	Methods				
		No Contact State	Location Point Cloud	Regress State	Contact Location Point Cloud	Ours
Single Object	Fixed Init - Translation Goal	<b>0.812 ± .012</b>	<b>0.973 ± .016</b>	<b>1.000 ± .000</b>	<b>0.996 ± .005</b>	<b>1.000 ± .000</b>
	Fixed Init - Any Goal	0.003 ± .000	0.020 ± .002	0.060 ± .014	<b>0.971 ± .005</b>	<b>0.982 ± .004</b>
	Any Init - Any Goal	0.000 ± .000	0.009 ± .001	0.573 ± .015	<b>0.991 ± .004</b>	<b>0.997 ± .003</b>
Cylindrical Objects	Fixed Init - Translation Goal	0.361 ± .019	0.107 ± .007	<b>0.990 ± .002</b>	<b>0.924 ± .027</b>	<b>0.961 ± .003</b>
	Fixed Init - Any Goal	0.001 ± .001	0.021 ± .002	0.264 ± .017	0.324 ± .014	<b>0.885 ± .004</b>
	Any Init - Any Goal	0.006 ± .002	0.035 ± .002	0.258 ± .010	0.187 ± .012	<b>0.879 ± .014</b>
All Objects	Any Init - Any Goal	0.005 ± .002	0.063 ± .007	0.037 ± .002	0.142 ± .009	<b>0.592 ± .020</b>

Table 6: **Ablations.** We show that all of the components are essential to achieve the best performance when the task becomes more difficult. Each success rate is reported with the mean and standard deviation across three seeds. Note that **Fixed Init - Translation Goal** and **Any Init - Any Goal** correspond to **Planar Goals** and **6D Goals** in Fig. 13 respectively.

Object Dataset	Task Configuration	Methods					
		Random Location	Greedy	No Flow (Goal PC)	No Flow (Goal Pose)	No Action Map	Ours
Single Object	Fixed Init - Translation Goal	0.323 ± .011	<b>1.000 ± .000</b>	<b>0.989 ± .002</b>	<b>1.000 ± .000</b>	<b>1.000 ± .000</b>	<b>1.000 ± .000</b>
	Fixed Init - Any Goal	0.075 ± .005	0.754 ± .023	0.198 ± .025	<b>1.000 ± .000</b>	<b>0.991 ± .002</b>	<b>0.982 ± .004</b>
	Any Init - Any Goal	0.037 ± .003	0.633 ± .014	0.181 ± .018	<b>0.994 ± .004</b>	<b>0.989 ± .002</b>	<b>0.997 ± .003</b>
Cylindrical Objects	Fixed Init - Translation Goal	0.158 ± .006	0.767 ± .017	<b>0.949 ± .003</b>	<b>0.927 ± .012</b>	<b>0.925 ± .012</b>	<b>0.961 ± .003</b>
	Fixed Init - Any Goal	0.097 ± .006	0.346 ± .012	0.189 ± .009	0.746 ± .015	0.805 ± .016	<b>0.885 ± .004</b>
	Any Init - Any Goal	0.093 ± .004	0.262 ± .011	0.216 ± .008	0.631 ± .016	0.775 ± .018	<b>0.879 ± .014</b>
All Objects	Any Init - Any Goal	0.181 ± .014	0.236 ± .005	0.209 ± .006	0.506 ± .007	<b>0.556 ± .015</b>	<b>0.592 ± .020</b>

### C.3 Generalization when trained on a single object

To further analyze the generalization of our method, we evaluate different policies over the “All Object” dataset when they are trained with a smaller dataset. In Fig. 16, we compare the performance of our method and the best baseline when trained only on a single object (blue dotted curve and orange dotted curve). The best baseline is “Regress Contact Location (Points)” according to Fig. 4. Although this baseline achieves a similar performance as our method on the single training object, it does not generalize as well as our method. When this baseline is trained with a more diverse object dataset, the performance becomes worse potentially due to the challenges in multi-task RL [38, 39]. In comparison, our method achieves better performance when trained on more diverse objects.

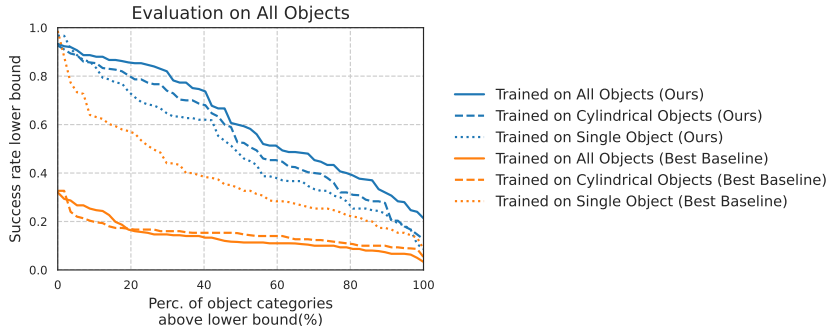


Figure 16: **Generalization to the full object dataset when trained on a smaller dataset.** The figure shows the evaluation performance over the “All Objects” dataset. Each curve represents the portion of the object categories that are above a certain success rate lower bound. A larger area under the curve means better performance across different objects.

### C.4 Per-category result breakdown

Fig. 17 shows the breakdown of the results for each object category. As mentioned in Section 7.2, the most difficult objects for this 6D pose alignment task are flat and thin objects while the easier ones have similar length along each dimension.

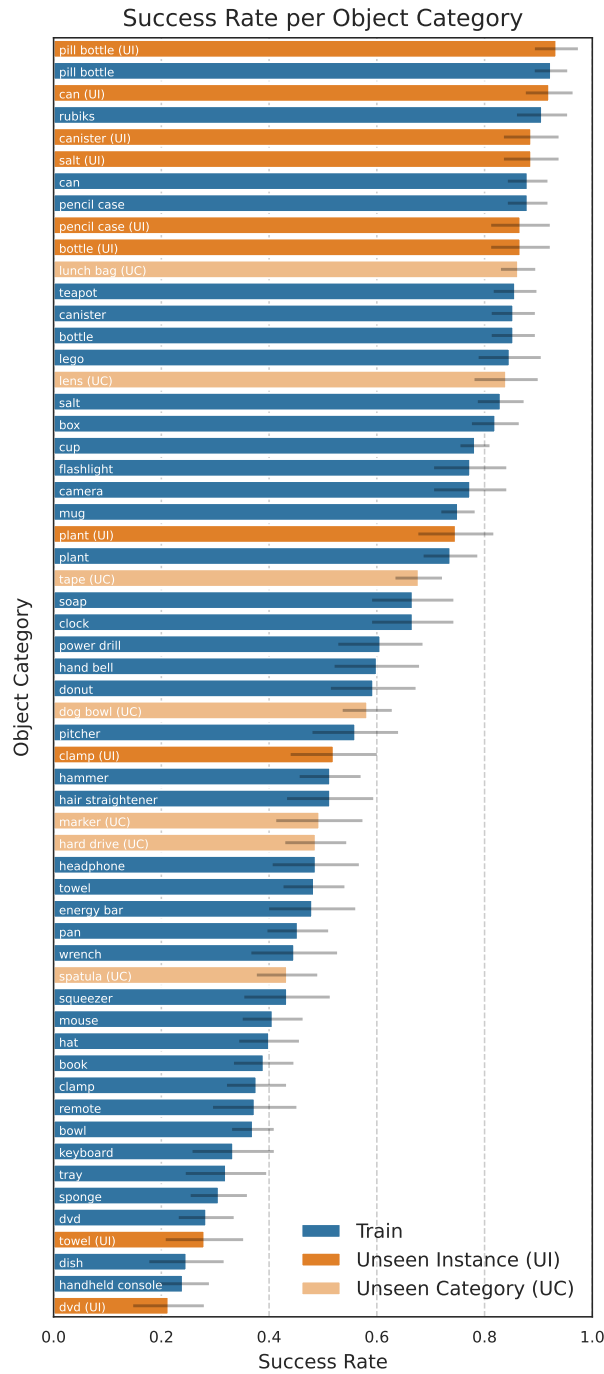


Figure 17: **Results breakdown.** Object categories in the unseen instance set (in orange) can be compared to the same object categories in the train set (in blue) to see the level of instance generalization.

## D Real Robot Experiments

### D.1 Real robot setup

The robot setup is shown in Fig. 18. We use three cameras on the real robot to get a combined point cloud. We follow a similar procedure as Appendix A to process the point cloud and to execute the action except the following details: We segment the object points from the full point cloud based on the location and the dimension of the bin instead of using the ground truth segmentation labels from Robosuite. To move the gripper to the pre-contact location, we first move the robot to a location above the pre-contact location and then move down to the pre-contact location, instead of “teleporting” the gripper in simulation.

To obtain goals for the real world evaluation, we record 10 goal point clouds for each object by manually setting the objects into different stable poses. During each timestep, we use point cloud registration algorithm to estimate the goal transformation to calculate the goal flow. Specifically, we use the global registration implementation from Open3D ([http://www.open3d.org/docs/release/tutorial/pipelines/global\\_registration.html](http://www.open3d.org/docs/release/tutorial/pipelines/global_registration.html)) and then use Iterative Closest Point (ICP) for local refinement. Note that we only match the shapes of the object instead of matching both the colors and the shapes due to the limitation of the registration algorithms.

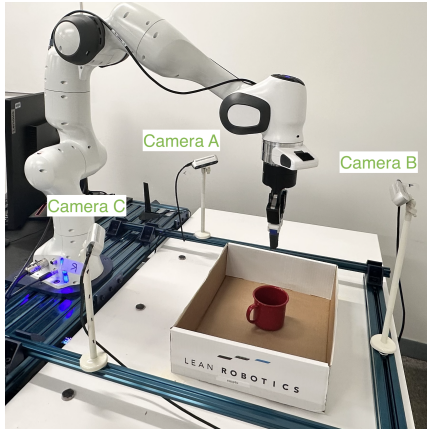


Figure 18: Real robot setup.

Note that the evaluation process can be done automatically without any manual resets. The reward and the episode termination condition (Appendix A.4) are both calculated automatically.

For the real robot experiments, we use the policy trained in the “6D goals” configuration with the “All Objects” dataset. We perform zero-shot sim2real transfer without finetuning or additional domain randomization. We have tried to add noise to the contact location execution and add noise to the point cloud observation. However, they did not result in better real robot performance.

### D.2 Analysis

We include additional analysis on the real robot results in this section. The proposed method assumes an estimated goal transformation as input. To estimate the transformation from the object to the goal, we use point cloud registration algorithms. However, the estimation of the transformation might not be perfect in the real world. To better understand the performance of our system, we define two types of evaluation criteria: The “flow success” is automatically calculated based on the estimated point cloud registration according to the evaluation metric in Appendix A.4. For the “actual success” evaluation metric, we manually mark as failures the cases among the flow success episodes where the goal estimation is significantly wrong. Thus, “flow success” indicates the performance of the trained policy while the “actual success” indicates the performance of the full system. Fig. 8 in the main text reports the actual success. We include both success metrics in Table 7 below. The policy achieves a 61% success rate based on the flow success.

### D.3 Failure cases

We discuss the failure cases of the real robot experiments in this section. The most noticeable failure cases are due to the errors of point cloud registration. The challenges of the registration methods come from noisy depth readings and partial point clouds. The error of the point cloud registration methods will lead to unexpected actions during the episode. In addition, it may end the episode early because the episode termination depends on the goal estimation. This motivates us to separate out the success criteria in Table 7 based on the failures of the registration method.

Table 7: **Additional analysis on the real robot experiments.** An episode is considered a “flow success” if the average norm of the estimated flow is less than 3 cm. An episode is considered as an “actual success” if the object is aligned with the goal pose without point cloud registration failure.

Object Name	Planar Goals		Non-planar Goals		Total	
	Flow	Actual	Flow	Actual	Flow	Actual
(a) Blue cup	4/7	4/7	7/13	4/13	5/20	4/20
(b) Milk carton	6/7	6/7	10/13	10/13	16/20	16/20
(c) Box	2/5	2/5	10/15	10/15	12/20	12/20
(d) Red bottle	7/7	4/7	6/13	0/13	13/20	4/20
(e) Hook	5/8	5/8	5/12	5/12	10/20	10/20
(f) Black mug	4/7	4/7	2/13	0/13	6/20	4/10
(g) Red mug	5/7	5/7	7/13	3/13	12/20	8/20
(h) Wood block	6/7	6/7	8/13	6/13	14/20	12/20
(i) Toy bridge	9/10	9/10	7/10	5/10	16/20	14/20
(j) Toy block	2/2	2/2	10/18	10/18	12/20	12/20
<b>Total</b>	50/67	47/67	72/133	53/133	122/200	100/200
<b>Percentage</b>	75%	70%	54%	40%	61%	<b>50%</b>

On the action side, both the contact location and the motion parameters might have execution errors. Since the contact location is selected from the observed point cloud, when the camera calibration is not accurate enough, the robot might not be able to reach the desired contact location of the object. In addition, since we use a compliant low-level controller to execute the motion parameters, they might not be able to execute the desired motion the same way as in simulation.

In addition, the object dynamics might be different from simulation due to the surface friction and the density of the object. The performance of our method could be further improved with domain randomization over the physical parameters.

## E More discussion on the related work

### E.1 Compared to Chen et al. [16, 17]

Our work is substantially different from Chen et al. [16, 17] from the follow aspects:

**Approach:** The approach in Chen et al. [16, 17] follows a student-teacher training pipeline. The teacher training is equivalent to the “No Contact Location” baseline with “states” observations in our paper. The policy takes all the relevant robot state and object state information and outputs delta robot actions. Note that they train a single teacher policy across all shapes without using the point cloud which results in a state-observation policy that is “robust” to shapes instead of “adaptive” to shapes (see Discussion section in Chen et al. [17]). As shown in Table II, this baseline performs significantly worse than our method in our task because it lacks shape information from the point cloud and the robot-centric action space is not as efficient as our object-centric action space. On the other hand, although the student policy in Chen et al. [16, 17] takes point cloud observation, its performance is upper bounded by the teacher policy which has been shown to be worse than our proposed method.

**Task:** We investigate a completely different task and thus the numbers are not really comparable with [16, 17]. First, we use a simple gripper instead of a dexterous hand. As mentioned in the discussion section of [17], “having more fingers can make it easier” to solve their task. Second, we consider matching the orientation and position of the goal pose while [16, 17] only considers orientation.

### E.2 Compared to Cheng et al. [1], Hou and Mason [2]

Unlike Cheng et al. [1], Hou and Mason [2], our method does not rely on quasi-static assumptions, is not limited to a simplified gripper model with a single point of contact, and does not require the knowledge of object environment contact modes which are challenging to estimate during real robot execution. As shown in our experiments, our approach exhibits superior motion complexity and object diversity compared to previous work.